Melting Behavior of Poly(ϵ-caprolactone)-*block*-Polybutadiene Copolymers

Shuichi Nojima,* Noriyuki Kikuchi, Awaludin Rohadi, Satoshi Tanimoto, and Shintaro Sasaki

School of Materials Science, Japan Advanced Institute of Science and Technology (JAIST), Tatsunokuchi, Ishikawa 923-1292, Japan

Received November 4, 1998; Revised Manuscript Received March 8, 1999

ABSTRACT: The melting behavior of poly(ϵ-caprolactone)-*block*-polybutadiene (PCL-*b*-PB) copolymers, crystallized at various temperatures T_c from the melt (homogeneous state or microphase-separated state), has been studied by small-angle X-ray scattering with synchrotron radiation (SR−SAXS). The strong SR−SAXS intensity peak changed into a sharp diffraction or a diffuse peak on heating, indicating a morphological transition from the lamellar morphology (an alternating structure consisting of crystallized lamellae and amorphous layers) into the microdomain structure or the homogeneous melt. The melting process of PCL-*b*-PB was extremely different from that of the poly(ϵ-caprolactone) (PCL) homopolymer; the long spacing of the lamellar morphology in PCL-*b*-PB, which depended significantly on T_c, remained constant or decreased slightly on heating, whereas that in PCL increased steadily. The morphological change in PCL-*b*-PB and PCL under the different thermal treatments was quantitatively investigated by SAXS and DSC. Details of the lamellar morphology initially formed in PCL-*b*-PB were determined mainly by the nonequilibrium crystallization of the PCL block at T_c, as in the case of PCL, but the subsequent heating did not alter this morphology, owing probably to the competition between the lamellar thickening and the contraction of the PB block existing between PCL lamellae, resulting in the characteristic melting behavior of PCL-*b*-PB.

1. Introduction

The crystallization behavior of block copolymers has been extensively studied during the past several years by using synchrotron radiation small-angle X-ray scattering (SR−SAXS) and wide-angle X-ray diffraction (SR−WAXD).[1−10] The characteristics of copolymer crystallization were elucidated for several systems such as poly(ϵ-caprolactone)-*block*-polybutadiene (PCL-*b*-PB),[1−3] polyethylene-*block*-poly(1-ethylethylene),[4−6,10] and poly(oxyethylene)-*block*-poly(oxybutylene).[7,9] It has been found from these studies that the crystallization process and final morphology relate intimately to the microdomain structure existing in the melt. In low-molecular-weight copolymers, for example, the microdomain structure is easily destroyed by the crystallization to result in a lamellar morphology, an alternating structure consisting of lamellae and amorphous layers, which is theoretically predicted to be the equilibrium morphology formed in crystalline−amorphous diblock copolymers.[11,12] This lamellar morphology was recently observed for a PCL-rich PCL-*b*-PB by transmission electron microscopy (TEM)[13] and confirmed for polyethylene-*block*-poly(ethylene-*alt*-propylene) (PE-*b*-PEP) even with a small PE fraction (∼0.12).[14]

When crystallized block copolymers are heated, we can observe the melting process in which the lamellar morphology is transformed into the microdomain structure. However, this is not the reverse process of the crystallization because lamellar morphology is kinetically formed under nonequilibrium crystallization and the various nonequilibrium lamellar morphologies are reorganized on heating toward a microdomain structure, an equilibrium morphology for low-molecular-weight block copolymers. There are, however, few studies on the melting process of crystalline−amorphous block copolymers.

The melting behavior of isothermally crystallized homopolymers has been one of the most extensively studied areas in the field of polymer science, and much information is available for the melting mechanism of crystalline homopolymers.[15−21] It is well-known from calorimetric studies that this mechanism is a multiple melting of lamellar morphology, in which thinner lamellae, formed under the nonequilibrium crystallization, melt and recrystallize on heating. Consequently, the long spacing of this lamellar morphology increases on heating, as revealed in the recent SR−SAXS studies[16,17] on the melting process of poly(aryl ether ether ketone).

In our earlier work,[22] we studied qualitatively the melting process of crystallized PCL-*b*-PB by SR−SAXS. Parameters characterizing the SR−SAXS curve, such as the peak intensity and position, were obtained as a function of temperature during heating, and the transition process (from the lamellar morphology into the microdomain structure) was phenomenologically observed from the change of these parameters only for limited conditions. In this work, we expanded the SR−SAXS study into various conditions to find the general picture of the melting behavior of PCL-*b*-PB, where we used various PCL-*b*-PB copolymers with the PCL volume fraction ranging from 0.10 to 0.61 and various crystallization temperatures T_c. In addition, we investigated the details of the lamellar morphology in PCL-*b*-PB formed under various thermal treatments by conventional SAXS (C−SAXS) and differential scanning calorimetry (DSC) to clarify the origin of the characteristic melting behavior of PCL-*b*-PB.

* Phone: +81-761-51-1601. Fax: +81-761-51-1149. E-mail: nojima@jaist.ac.jp.

10.1021/ma981708p CCC: $18.00
Published on Web 05/07/1999

Table 1. Characterization of Polymers Used in This Study

sample code	polymer	source	Total M_n	M_w/M_n[a]	PCL/PB[b] (vol %)	Microstructure of PB chain[b] (%)			T_m[c] (°C)
						cis-1,4	*trans*-1,4	1,2-linkage	
CL61	PCL-*b*-PB	[d]	12 400[e]	1.10	61:39	36	52	12	54
CL26	PCL-*b*-PB	[d]	14 000[e]	1.09	26:74	35	51	14	45
CL19	PCL-*b*-PB	[d]	11 000[f]	1.19	19:81	34	49	17	50
CL10	PCL-*b*-PB	[d]	14 000[f]	1.10	10:90	37	50	13	43
CL100	PCL	[g]	7 000[f]	1.57					57

[a] Determined by GPC. [b] Determined by ^{1}H NMR. [c] Determined by DSC at a heating rate of 5 °C/min. [d] Synthesized in our laboratory. [e] Determined by GPC with PS as a standard. [f] Determined by VPO. [g] Obtained from Scientific Polymer Products, Inc.

2. Experimental Section

2.1. Materials. PCL-*b*-PB copolymers used in this study were synthesized by a successive anionic polymerization under vacuum. Details of the synthesis are described elsewhere.[1,13,23] The block copolymers obtained were characterized by gel permeation chromatography (GPC), vapor pressure osmometry (VPO), nuclear magnetic resonance (^{1}H NMR), and DSC. The results of molecular characterization are shown in Table 1, where the numeral after "CL" in the sample code represents the volume percentage (vol %) of PCL blocks in the copolymer. The following specific volumes were used to calculate the volume fraction of each block from ^{1}H NMR results and to evaluate the electron density necessary for the quantitative analysis of SR−SAXS curves. For polybutadiene[24]

$$v_{sp}(T) = 1.1138 + (8.24 \times 10^{-4})T \quad (1)$$

and for amorphous poly(ϵ-caprolactone)[25]

$$v_{sp}(T) = 0.9106 + (6.013 \times 10^{-4})T \quad (2)$$

where $v_{sp}(T)$ is in cubic centimeters per gram and T is in degrees Celcius. For the perfect crystal of PCL, $v_{sp} = 0.833$ cm^3/g was used irrespective of temperature.[26]

2.2. DSC Measurements. A Perkin−Elmer Pyris 1 DSC was used to evaluate the melting temperature of PCL blocks T_m and PCL crystallinity χ_w (i.e., the weight fraction of the crystallized PCL block against the total PCL block existing in the system). T_m was defined as the temperature at which the endothermic peak was maximum, and χ_w was calculated from the peak area ΔH by

$$\chi_w = \Delta H/(\Delta H^\circ f_w) \quad (3)$$

where f_w is the weight fraction of PCL blocks in the copolymer and ΔH° is the heat of fusion for perfect PCL crystals (ΔH° = 135.44 J/g[25]). The heating rate was 5 or 2 °C/min; the latter was the heating rate when the melting behavior was observed by SR−SAXS.

2.3. SAXS Measurements. We used two SAXS techniques in this study: time-resolved SAXS employing synchrotron radiation for the observation of melting processes and conventional SAXS for the morphological investigation.

The SR−SAXS experiment was performed at Institute of Materials Structure Science, Tsukuba, Japan (Photon Factory), with small-angle X-ray equipment for solution (SAXES) installed on a beam line BL-10C. Details of the optics and the instrumentation are described elsewhere.[27] The sample temperature was controlled by circulating water supplied by a programmable water bath. The sample was first annealed at ca. 65 °C for 30 min to erase the previous thermal history and to develop the microdomain structure; it was then quenched into the crystallization temperature T_c by dropping the water temperature, kept at T_c for 30−100 min to observe the crystallization process by SR−SAXS, and finally heated at a constant heating rate (ca. 2 °C/min) until the sample was completely melted during which the melting process was also observed by SR−SAXS. Crystallization of CL10 at each T_c was carried out in advance because it took too long to be pursued by SR−SAXS, and we put the crystallized CL10 in the sample holder to observe only the melting process. The integrated SAXS intensity was monitored during the crystallization and melting processes, which enabled us to proceed to the next step in the temperature program. The SAXS intensity was collected as an accumulation of the scattered intensity during 10 s for both the crystallization and melting processes and corrected for a minor decrease in the ring current during measurements, which was continuously monitored by an ionization chamber placed just before the sample. In this manuscript, we focus our attention only on the melting process because the crystallization process already was reported.[1−3]

The C−SAXS experiment was performed with point focusing optics and a one-dimensional position sensitive proportional counter (PSPC) with an effective length of 10 cm.[28] Cu Kα radiation supplied by a MAC Science M18X generator operating at 40 kV and 30 mA was used. The accumulation time for each measurement was 3000−5000 s depending on the scattered intensity from the sample.

The SAXS curve measured by both SR−SAXS and C−SAXS was corrected for background scattering and absorption of the sample. Because SR−SAXS and C−SAXS are from the *point* focusing, the scattered intensity was not corrected for the smearing effect by the finite cross section of the primary beam. The SAXS curve was finally obtained as a function of s defined by

$$s = 2 \sin \theta/\lambda \quad (4)$$

where 2θ is the scattering angle and λ is the X-ray wavelength used (λ = 0.1488 nm for SR−SAXS and 0.1542 nm for C−SAXS).

2.4. Analysis of SR−SAXS Curves. All SR−SAXS curves observed for CL19, CL26, and CL61 had an intensity peak arising from the lamellar morphology, microdomain structure, or a combination of these morphologies. The SR−SAXS curve for CL10 had a weak intensity peak at temperatures above T_m, and that of CL100 decreased monotonically with increasing s at temperatures above T_m. We first evaluated the temperature dependence of the angular position of the SAXS peak, where SAXS intensity was multiplied by the Lorentz factor ($4\pi^2 s^2$) in expectation of the lamellar morphology for crystallized samples.

Next we calculated the temperature dependence of the invariant $Q(T)$ defined by

$$Q(T) = \int_0^\infty s^2 I(s)\, ds \quad (5)$$

which gives information about the morphology during melting and relates to a mean square fluctuation of the electron density $\langle \Delta\rho^2 \rangle$ in the system through

$$Q(T) = K\langle \Delta\rho^2 \rangle \quad (6)$$

where K is a constant relating to the X-ray irradiated volume. In performing the integration of eq 5, the intensity at high scattering angles was necessary. The SR−SAXS curve was, however, limited to a finite angle ($s \leq 0.3$ nm^{-1}) owing to the fixed geometry of the apparatus. When the scattering data in the wide-angle region are not available, such as in the present study, the background scattering I_b can be considered constant and the scattered intensity is approximated by Porod's law extrapolation expressed as[29,30]

$$I(s)s^4 = \text{constant} + I_b s^4 \quad (7)$$

The slope of the expected straight line in the plot of $I(s)s^4$ versus s^4 gives I_b arising from the composition fluctuation.

When we consider the melting process of crystallized PCL blocks, three phases (PCL crystal, amorphous PCL phase, and amorphous PB phase) are expected to appear in the system if we assume that PB blocks segregate completely from amorphous PCL blocks. $<\Delta\rho^2>$ of the ternary system is given by[30]

$$\langle\Delta\rho^2\rangle = (\rho_{PB} - \rho_{PCL,a})^2(1 - f_v)f_v(1 - \chi_v) + (\rho_{PB} - \rho_{PCL,c})^2(1 - f_v)f_v\chi_v + (\rho_{PCL,a} - \rho_{PCL,c})^2 f_v^2\chi_v(1 - \chi_v) \quad (8)$$

where ρ_{PB}, $\rho_{PCL,a}$ and $\rho_{PCL,c}$ are electron densities of PB blocks, amorphous PCL blocks, and perfect PCL crystals, respectively, f_v the volume fraction of PCL blocks in the system, and χ_v the volume fraction of crystallized PCL blocks against total PCL blocks in the system, which is roughly equal to χ_w defined by eq 3. When the PCL crystal melts completely at T_m (i.e., $\chi_v = 0$), the three-phase structure reduces to the two-phase structure (microdomain structure) consisting of PB blocks and amorphous PCL blocks, and $Q(T)$ at $T > T_m$, Q_f, can be given by

$$Q_f = K(\rho_{PB} - \rho_{PCL,a})^2(1 - f_v)f_v \quad (9)$$

By combining eqs 6, 8, and 9, $Q(T)$ can be expressed as

$$\frac{Q(T)}{Q_f} = 1 - \chi_v + \left(\frac{\rho_{PB} - \rho_{PCL,c}}{\rho_{PB} - \rho_{PCL,a}}\right)^2\chi_v + \left(\frac{\rho_{PCL,a} - \rho_{PCL,c}}{\rho_{PCL,a} - \rho_{PB}}\right)^2\frac{\chi_v(1 - \chi_v)f_v}{1 - f_v} \quad (10)$$

By solving above quadratic equation for χ_v, we can evaluate χ_v as a function of T during melting. This gives direct evidence for how χ_v (or χ_w) changes with increasing T. Note that eq 10 cannot be applied for CL100 because we cannot evaluate K in eq 9 from the fact that the molten CL100 has no definite morphology to yield $Q_f = 0$.

2.5. Morphological Study Formed in CL19 and CL100. On the basis of SR−SAXS results, we investigated the details of the morphology formed in CL19 and CL100 by applying various thermal treatments. CL19 was chosen on behalf of all copolymers because the absolute molecular weight was known (Table 1), and the PCL crystallinity χ_w was easily evaluated from DSC measurements. The sample was first annealed at ca. 65 °C for 30 min, quenched into T_c ranging from 12 to 30 °C for CL19 and 33 to 49 °C for CL100 to crystallize the sample for 10−24 h, heated to $T_{c,f}$ ($< T_m$, $T_{c,f}$ = 30 °C for CL19 and $T_{c,f}$ = 49 °C for CL100) at ca. 2 °C/min, and finally annealed at $T_{c,f}$ for 24 h. C−SAXS and DSC measurements were performed to find the difference in the morphology at $T_{c,f}$ as a function of T_c or ΔT (= $T_c - T_{c,f}$). That is, by assuming the lamellar morphology with a sharp interface between the lamella and amorphous layer, we calculated the lamellar thickness L_c and amorphous layer thickness L_a as a function of ΔT from the long spacing L (C−SAXS) and χ_w (DSC) by

$$L_c = L\,\chi_w \quad (11)$$

$$L_a = L(1 - \chi_w) \quad (12)$$

where χ_w was not converted into χ_v because the difference was small. It is reasonable to assume the lamellar morphology for CL19 because this morphology was already observed for block copolymers even with a small crystallizable fraction (∼0.12).[14]

3. Results and Discussion

3.1. Melting Process of PCL-*b*-PB. 3.1.1. Overview of SR−SAXS Curves. Figure 1 shows the typical SR−SAXS curves obtained for (a) CL10 and (b) CL26 during heating. At the beginning of heating, a strong SAXS intensity peak from the lamellar morphology appears and decreases gradually in intensity with increasing temperature T. In contrast to other block copolymers,[4,5] no higher-order SAXS peak was observed, which may be attributed to the polydispersity of the PCL block owing to the inevitable side-reactions during polymerization. The peak becomes extremely broad at temperatures just before the melting of PCL blocks (indicated by an arrow in Figure 1a), and eventually, a diffuse peak (Figure 1a) or sharp diffraction (Figure 1b) emerges at a higher angle from this broad peak. The broad peak in the intermediate stage is characteristic of the melting process of PCL-*b*-PB and it was never observed in the crystallization process, where two intensity peaks (arising from the microdomain structure and lamellar morphology) changed independently with crystallization time.[1,3] The diffuse peak after melting arises from the composition fluctuation in the homogeneous CL10 melt (correlation hole effect[31]), and the sharp diffraction is due to the microdomain structure formed in the CL26 melt. CL19 and CL61 had similar sharp diffractions after melting, indicating that they form the microdomain structure. The compositional asymmetry will be responsible for the morphological difference in the melt.[32] The SR−SAXS curves shown in Figure 1 were reproducible even if the thermal

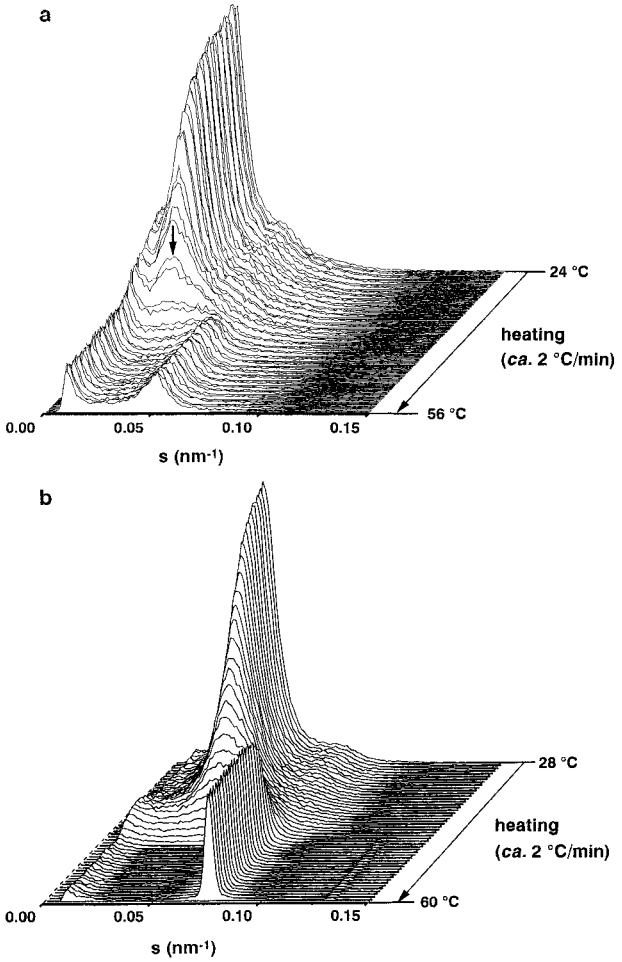

Figure 1. Overview of three-dimensional SR−SAXS curves for (a) CL10 and (b) CL26 on heating. The abscissa is the wavenumber s defined by eq 4 and the ordinate (intensity) is in an arbitrary scale. The arrow in part a shows the intermediate stage of melting, where the SAXS intensity peak becomes extremely broad.

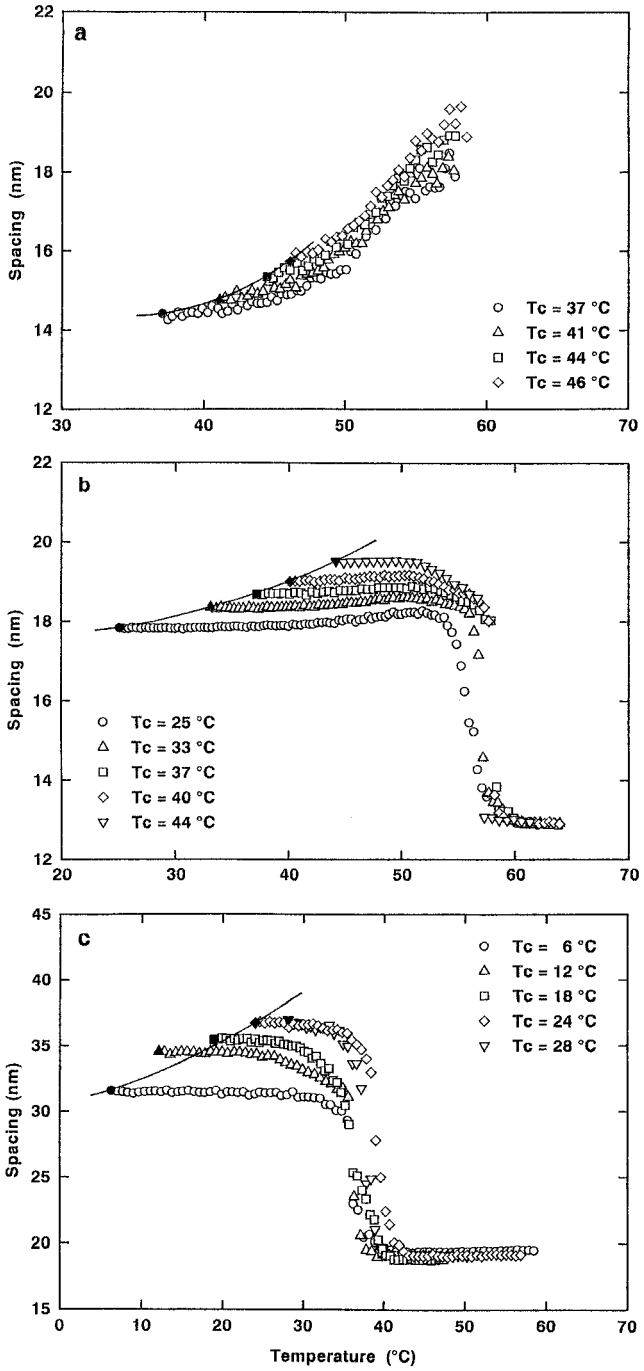

Figure 2. Temperature dependence of the spacing for (a) CL100, (b) CL61, and (c) CL10 crystallized at each T_c indicated. The closed symbol represents the initial value of L for each T_c from which it begins to change on heating. The solid curve represents the plot of L vs T_c.

history was repeatedly applied. In addition, the difference in the heating rate did not alter the features of SR−SAXS curves and, therefore, the main results obtained when it was in the range between 0.9 and 3.0 °C/min. We used ca. 2 °C/min for all of the heating measurements.

3.1.2. Temperature Dependence of SR−SAXS Curves. The long spacing L, evaluated from the angular position of the SR−SAXS peak during heating, is shown in Figure 2 for (a) CL100, (b) CL61, and (c) CL10 crystallized at each T_c indicated. The closed symbol in each figure represents the initial position of L when the sample is quenched into T_c, from which L begins to change on heating. That is, the curve connecting these symbols (solid curve) represents the plot of L versus T_c.

The initial L for CL100 (closed symbols in Figure 2a) becomes larger with increasing T_c, which is well-known for crystalline homopolymers.[33] That is, owing to the slow crystallization at higher T_c, the number of chain folds reduces to result in thicker lamellae and eventually larger L. L for CL100 begins to increase monotonically on subsequent heating with a shape similar to the solid curve and finally disappears at T_m. As a result, the L versus T plot (Figure 2a) makes a master curve in which T_c does not significantly affect L at a given T. The increase of L is usually observed in the heating measurement of crystalline homopolymers,[15−21] which can be explained by the lamellar thickening mechanism; i.e., thin lamellae, formed under the nonequilibrium crystallization at T_c, melt and recrystallize during heating to yield thicker lamellae. The T dependence of L for CL61 and CL10 (Parts b and c of Figure 2) is, on the other hand, extremely different from that for CL100. L remains constant or decreases slightly on heating though the initial L (closed symbols in Figure 2b,c) is strongly dependent on T_c, as observed for many diblock copolymers.[1,6,9] L turns into a small value at T_m, indicating a morphological transition from the lamellar morphology into the microdomain structure (CL61) or homogeneous melt (CL10). This T dependence of L makes the difference in the absolute value of L larger at a given T ($< T_m$) among the samples crystallized at different T_c. Figure 2c, for example, shows that CL10 crystallized at 6 °C has $L \approx 32$ nm and keeps this value constant during heating to have $L \approx 32$ nm at 28 °C, whereas CL10 directly crystallized at $T_c = 28$ °C has $L \approx 37$ nm. The difference in L is 5 nm at 28 °C between CL10 crystallized at $T_c = 6$ and 28 °C.

The characteristic change in L could be observed for other block copolymers; that is, L never increased on heating for all cases. It is easily understandable that the melting process of block copolymers (CL10, CL19, CL26, and CL61) is extremely different from that of crystalline homopolymers (CL100). We further analyze the SR−SAXS curves on the basis of $Q(T)$ to clarify the melting behavior of PCL-*b*-PB.

3.1.3. Temperature Dependence of $Q(T)$ and χ_v. The invariant $Q(T)$, evaluated from each SR−SAXS curve through eqs 5−7, remained constant on heating and eventually decreased smoothly at around T_m toward a final value, Q_f. The T dependence of $Q(T)$ was similar irrespective of PCL-*b*-PB and T_c.

The PCL crystallinity χ_v of CL61 and CL10, evaluated from $Q(T)$ by eq 10, is plotted against T in Figure 3. χ_v first decreases slightly with increasing T followed by an abrupt decrease at around T_m with a finite melting width. The thermal expansion of the amorphous PCL and PB blocks is mainly responsible for the slight decrease in χ_v before melting, because we obtained an almost constant χ_v during heating if we ignored the T dependence of specific volume for the amorphous PCL and PB blocks (eqs 1 and 2). Figure 3 shows that there is a finite melting zone, χ_v decreases linearly with T within this zone, and finally the system changes into the microdomain structure (CL61) or the homogeneous melt (CL10).

We characterized the melting zone by approximating the change in χ_v with three lines, as depicted in Figure 3a. Two characteristic temperatures of this melting process, T_h and T_l, were obtained, and the melting

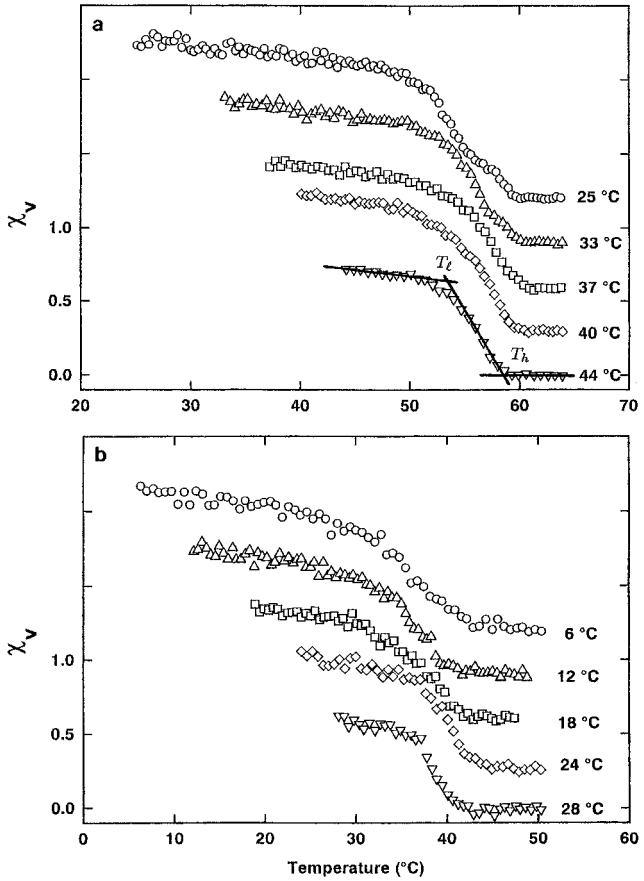

Figure 3. Temperature dependence of χ_v evaluated from $Q(T)$ by eq 10 for (a) CL61 and (b) CL10 crystallized at each T_c indicated. The data points except 44 °C in part a and 28 °C in part b are shifted upward successively for legibility.

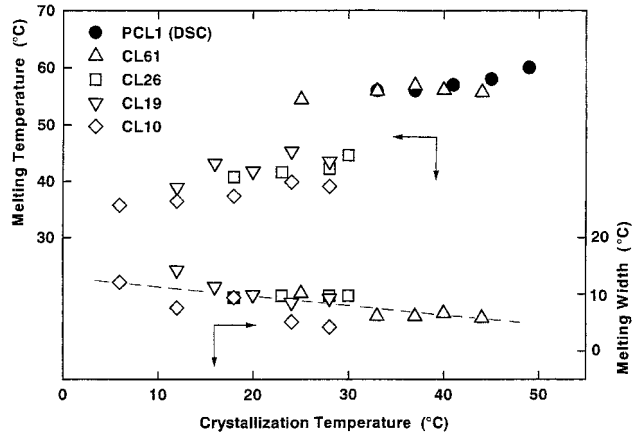

Figure 4. T_c dependence of melting temperature T'_m and melting width Δw evaluated from Figure 3 for CL61 (△), CL26 (□), CL19 (▽), and CL10 (◇). T_m measured by DSC for PCL1 is also shown (●).

temperature T'_m was evaluated from an average of T_h and T_l and the melting width Δw from $T_h - T_l$. The plots of T'_m and Δw against T_c are shown in Figure 4, where the results of all the block copolymers are plotted, together with T_m for CL100 measured by DSC. Each T'_m increases with increasing T_c with the slope ranging from 0.08 (CL61) to 0.28 °C/°C (CL19). This slope is comparable to or lower than that of CL100 measured by DSC (0.25 °C/°C) and the result by Phillips et al. for PCL (0.27 °C/°C).[34] Δw decreases slightly with increasing T_c with no definite difference among copolymers.

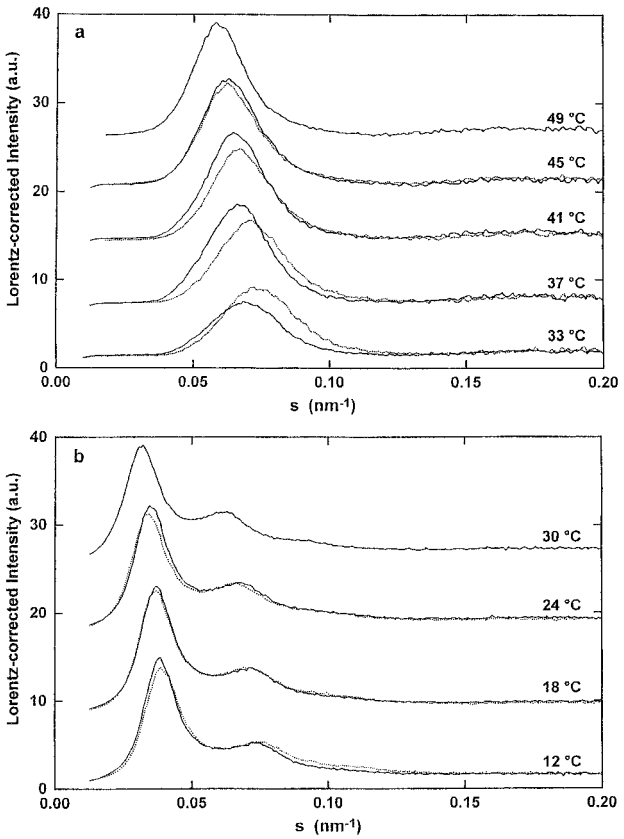

Figure 5. Lorentz-corrected SAXS intensity plotted against s for (a) CL100 and (b) CL19. The dotted curves were measured after the sample was directly crystallized at T_c for 24 h, and the solid curves were measured after the sample was crystallized at T_c followed by heating to $T_{c,f}$ (49 °C for CL100 and 30 °C for CL19).

It has been generally observed for crystalline homopolymers that the lamellar thickness increases with increasing T_c to yield a higher T_m, that is; T_m increases steadily with increasing T_c. The regularity of the lamellar morphology has also been observed to increase with increasing T_c because of slower crystallization; that is, Δw decreases gradually with increasing T_c. Therefore, Figure 4 is reminiscent of homopolymer melting; the morphology formation in PCL-*b*-PB seems to be mainly driven by the nonequilibrium crystallization of the PCL block at T_c, and it is no matter whether the PCL chain participating in the crystallization is a part of block copolymers or homopolymers.

In summary, SR−SAXS measurements have revealed that the melting behavior of PCL-*b*-PB is unique. In particular, the T dependence of L is extremely different from that of CL100 (Figure 2); L in PCL-*b*-PB, which depended significantly on T_c, remained constant or decreased slightly on heating, whereas L in PCL increased steadily.

3.2. Lamellar Morphology Formed in CL100 and CL19. 3.2.1. C−SAXS and DSC Results. On the basis of SR−SAXS results, the lamellar morphology formed in CL100 and CL19 was quantitatively investigated by applying various thermal histories described in the Experimental Section. Figure 5 shows C−SAXS curves for (a) CL100 and (b) CL19 crystallized at each T_c indicated (dotted curves) and those crystallized at T_c followed by heating to $T_{c,f}$ (solid curves). As expected from Figure 2a, the angular position of the SAXS peak for CL100 shifts significantly to the smaller angle by

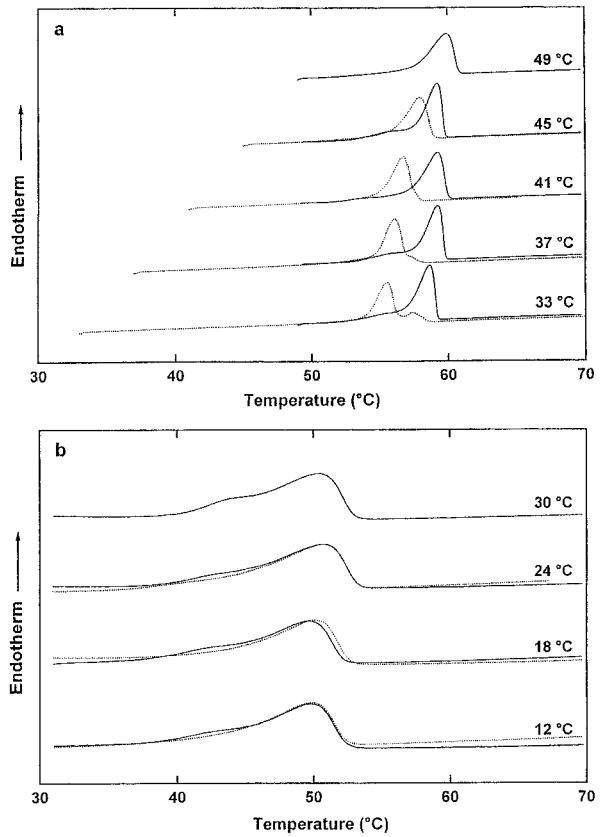

Figure 6. DSC curves for (a) CL100 and (b) CL19. The dotted curves were measured after the sample was crystallized at T_c for 24 h, and the solid curves were measured after the sample was crystallized at T_c followed by heating to $T_{c,f}$ (49 °C for CL100 and 30 °C for CL19). The heating rate is 5 °C/min.

heating. It is, therefore, difficult to control the lamellar morphology formed in CL100 by changing T_c, because the subsequent heating leads to an appreciable increase of L. On the other hand, C−SAXS curves for CL19 are unchanged by the thermal treatment and the difference in the *absolute value* of L is extremely large between the samples directly crystallized at $T_{c,f}$ and those crystallized at T_c ($< T_{c,f}$) followed by heating to $T_{c,f}$. That is, the lamellar morphology formed in CL19 is strongly path-dependent (or T_c-dependent), so that it seems possible to control the long spacing formed at $T_{c,f}$ by changing T_c applied to the sample in advance.

Figure 6 shows DSC curves for CL100 and CL19, where the thermal history applied is the same as that applied to the sample in Figure 5. DSC curves for CL100 (Figure 6a) change significantly by the subsequent thermal treatment; in particular, T_m shifts remarkably toward the higher temperature, which indicates lamellar thickening during heating.[33] The DSC curves for CL19 (Figure 6b) are, on the other hand, almost unchanged, suggesting constant lamellar thickness during thermal treatment, although the temperature span of the peak is much wider (>12°C). Figures 5 and 6 show that the lamellar morphology formed in CL19 at T_c is practically unchanged after heating and annealing at $T_{c,f}$, and similar results were obtained for CL10, CL26, and CL61. This difference between CL100 and CL19 should relate to the change in the lamellar thickness L_c and amorphous layer thickness L_a during heating and annealing at $T_{c,f}$, and we evaluate these values from the combination of C−SAXS and DSC results.

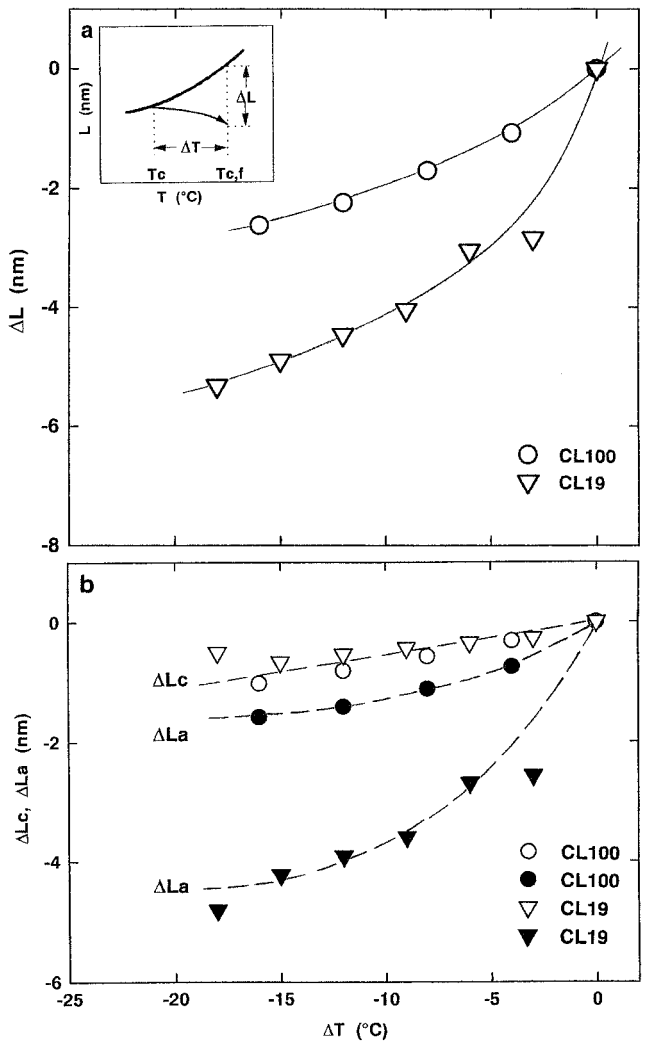

Figure 7. (a) ΔL plotted against the temperature difference ΔT ($= T_c - T_{c,f}$), where ΔL represents the difference in the long spacing between the samples directly crystallized at $T_{c,f}$ and those crystallized at T_c followed by heating to $T_{c,f}$. The inset represents the definition of ΔL and ΔT. (b) The difference in the lamellar thickness ΔL_c and amorphous layer thickness ΔL_a plotted against ΔT for CL100 (○ and ●) and CL19 (▽ and ▼).

3.2.2. Lamellar Thickness and Amorphous Layer Thickness. Figure 7a shows the difference in the long spacing ΔL between the samples directly crystallized at $T_{c,f}$ and those crystallized at T_c followed by heating to $T_{c,f}$ as a function of the temperature difference ΔT ($= T_c - T_{c,f}$). Because the C−SAXS and DSC measurements were performed for the samples finally annealed at $T_{c,f}$ for 24 h, the negative value of ΔL arises only from the difference in T_c (or ΔT). Note that ΔL should be 0 at $\Delta T = 0$. Figure 7a indicates that when CL100 is heated from T_c to $T_{c,f}$, L does not recover completely (the amount of which depends on T_c). This indicates that the lamellar morphology formed in CL100 is, strictly speaking, *path-dependent*, which is expected from Figure 2a. ΔL for CL19 is, on the other hand, strongly dependent on T_c (or ΔT).

To understand the difference in the magnitude of ΔL between CL100 and CL19, the contributions of L_c and L_a to ΔL, ΔL_c, and ΔL_a, were estimated through eqs 11 and 12, and plotted in Figure 7b. The magnitude of ΔL_c is similar for both cases, but the relative change of ΔL_c for CL100 is significantly smaller than that for CL19

(for example, 8.4% and 14.2% at $\Delta T = -12$ °C). This is mainly ascribed to the lamellar thickening in CL100 during heating. Figure 7b also shows that ΔL_a contributes predominantly to ΔL in CL19.

It was found in the previous section that in the case of PCL-*b*-PB L remained constant or decreased slightly (Figure 2b,c) and T_m (and hence lamellar thickness) was also unchanged (Figure 6b) during heating. These facts make us speculate that both L_c and L_a remain constant or decrease slightly during heating. That is, the major difference in the lamellar morphology between the samples directly crystallized at $T_{c,f}$ (=30 °C) and those crystallized at T_c ($< T_{c,f}$) and subsequently heated to $T_{c,f}$ originates from the difference in the morphology formed at T_c and $T_{c,f}$; i.e, the heating process does not alter the morphology of PCL-*b*-PB substantially, which is extremely different from the case of PCL. This difference between PCL and PCL-*b*-PB should be related to the existence of PB blocks accommodated between PCL lamellae. In the lamellar morphology of PCL-*b*-PB, the PB block will be elongated more or less on the direction perpendicular to the lamellar surface because the nonequilibrium crystallization of the PCL block drives the morphology formation at T_c, where the amorphous layer thickness (or the degree of elongation of PB blocks) is regulated by the lamellar thickness. The PB blocks tend to contract rather than elongate on heating because a random-coil conformation is favorable to the amorphous chain. This is incompatible with the lamellar thickening of the PCL block during heating because it leads to the further elongation of the PB block. Therefore, there is a competition between the lamellar thickening and the contraction of the PB block during heating, and a subtle balance between them will make the lamellar morphology unchanged. As a result, there is no recovery of L_c and L_a after heating and a large ΔL_a remains at $T_{c,f}$. This effect does not work in homopolymer melting, and ΔL_c increases and ΔL_a decreases for CL100 on heating.

In summary, the existence of PB blocks in the lamellar morphology yields the characteristic melting behavior of PCL-*b*-PB, which cannot be observed for the melting of crystalline homopolymers. The evaluation of the conformation of the PCL and PB blocks formed at T_c is necessary to confirm the above discussion and is useful for further understanding of the morphological change during heating.

3.2.3. Conformation of PCL and PB Blocks. When we consider the detailed lamellar morphology formed at T_c, L_a should relate intimately to L_c because the folding of the PCL block provides the space available for the accommodation of the PB block and, consequently, controls the conformation of the PB block. Here, we consider (1) the number of PCL chain folds and (2) the degree of elongation of the PB block in the lamellar morphology formed at T_c.

The monomer number n composed of one stem in PCL lamellae is calculated from the crystal structure of PCL[35] if we assume that the stem is perpendicular to the lamellar surface. Because the unit cell of PCL crystals contains two chains consisting of two monomers with $c = 1.705$ nm, n is given by

$$n = \frac{2\,L_c}{1.705} \tag{13}$$

The number of chain folds n_f on the lamellar surface for CL19 with n is

$$n_f = \frac{M_{PCL} \times f_n}{M_0 \times n} - 1 \tag{14}$$

where M_{PCL} is the molecular weight of the PCL block in CL19 (=2600 g/mol), M_0 is that of the ϵ-caprolactone (CL) monomer (=114 g/mol), and f_n is the mole fraction of crystallized CL monomers against total CL monomers. n_f thus evaluated is between 2.0 and 2.8 and smoothly decreases with increasing ΔT; that is, n_f increases with decreasing T_c. We cannot observe the quantization of n_f, as observed in other block copolymers.[7,9] This also suggests that the lamellar morphology is determined by the nonequilibrium crystallization at T_c, as in the case of crystalline homopolymers.

The diameter of the PB block in the unperturbed state, d, can be calculated from the end to end distance of PB homopolymers by[13]

$$d = \frac{2a}{\sqrt{6}} M_{PB}^{1/2} \tag{15}$$

where a is in the range between 0.082 and 0.103 nm depending on the microstructure of the PB block (cis, trans, or 1,2-linkage) and M_{PB} is the molecular weight of the PB block in CL19 (=8400 g/mol). d is calculated to be 6.1−7.7 nm for the PB block in CL19. If we assume a single-layer model for the lamellar morphology,[12] we can calculate the size of the PB block d' in the direction normal to the lamellar surface from L_a and χ_v. The ratio of d' against d gives the degree of elongation of the PB block in the lamellar morphology. d'/d is evaluated to be 1.36 at $\Delta T_c = -18$ °C in the smallest case (i.e., $a =$ 0.103 nm) and increases slightly with increasing T_c. That is, when PCL-*b*-PB crystallizes at T_c the PB block is somewhat elongated in the direction normal to the lamellar surface and the degree of elongation increases with increasing T_c. This supports our previous discussion about the characteristic melting behavior of PCL-*b*-PB. That is, the lamellar thickening during heating leads to further elongation of the PB block, which will not be favorable to the whole system.

Acknowledgment. This work was supported in part by Tokuyama Science Foundation and by Grants-in-Aid for Scientific Research (No. 09650992) from the Ministry of Education, Science, Sports, and Culture of Japan and has been performed under the approval of the Photon Factory Program Advisory Committee (No. 97G229).

References and Notes

(1) Nojima, S.; Kato, K.; Yamamoto, S.; Ashida, T. *Macromolecules* **1992**, *25*, 2237.
(2) Nojima, S.; Nakano, H.; Ashida, T. *Polym. Commun.* **1993**, *34*, 4168.
(3) Nojima, S.; Nakano, H.; Takahashi, Y.; Ashida, T. *Polymer* **1994**, *35*, 3479.
(4) Rangarajan, P.; Register, R. A.; Adamson, D. H.; Fetters, L. J.; Bras, W.; Naylor, S.; Ryan, A. J. *Macromolecules* **1995**, *28*, 1422.
(5) Ryan, A. J.; Hamley, I. W.; Bras, W.; Bates, F. S. *Macromolecules* **1995**, *28*, 3860.
(6) Rangarajan, P.; Register, R. A.; Fetters, L. J.; Bras, W.; Naylor, S.; Ryan, A. J. *Macromolecules* **1995**, *28*, 4932.
(7) Yang, Y. W.; Tanodekaew, S.; Mai, S. M.; Booth, C.; Ryan, A. J.; Bras, W.; Viras, K. *Macromolecules* **1995**, *28*, 6029.
(8) Quiram, D. J.; Register, R. A.; Marchand, G. R.; Ryan. A. J. *Macromolecules* **1997**, *30*, 8338.

(9) Mai, S. M.; Fairclough, J. P. A.; Viras, K.; Gorry, P. A.; Hamley, I. W.; Ryan, A. J.; Booth, C. *Macromolecules* **1997**, *30*, 8392.
(10) Hamley, I. W.; Fairclough, J. P. A.; Bates, F. S.; Ryan, A. J. *Polymer* **1998**, *39*, 1429.
(11) DiMarzio, E. A.; Guttman, C. A.; Hoffmann, J. D. *Macromolecules* **1980**, *13*, 1194.
(12) Whitmore, M. D.; Noolandi, J. *Macromolecules* **1988**, *21*, 1482.
(13) Nojima, S.; Yamamoto, S.; Ashida, T. *Polym. J.* **1995**, *27*, 673.
(14) Rangarajan, P.; Register, R. A.; Fetters, L. J. *Macromolecules* **1993**, *26*, 4640.
(15) Schouterden, P.; Vandermarliere, M.; Riekel, C.; Koch, M. H. J.; Groeninckx, G.; Reynaers, H. *Macromolecules* **1989**, *22*, 237.
(16) Hsiao, B. S.; Gardner, K. H.; Wu, D. Q.; Chu, B. *Polymer* **1993**, *34*, 3996.
(17) Kruger, K. N.; Zachmann, H. G. *Macromolecules* **1993**, *26*, 5202.
(18) O'kane, W. J.; Young, R. J.; Ryan, A. J.; Bras, W.; Derbyshire, G. E.; Mant, G. R. *Polymer* **1994**, *35*, 1352.
(19) Verma, R. K.; Velikov, V.; Kander, R. G.; Marand, H.; Chu, B.; Hsiao, B. S. *Polymer* **1996**, *37*, 5357.
(20) Rodriguez, F. J. M.; Phillips, P. J.; Lin, J. S. *Macromolecules* **1996**, *29*, 7491.
(21) Ryan, A. J.; Stanford, J. L.; Bras, W.; Nye, T. M. W. *Polymer* **1997**, *38*, 759.
(22) Nojima, S.; Kanda, Y.; Sasaki, S. *Polym. J.* **1998**, *30*, 628.
(23) Nojima, S.; Wang, D.; Ashida, T. *Polym. J.* **1991**, *23*, 1473.
(24) Rigby, D.; Roe, R. J. *Macromolecules* **1986**, *19*, 721.
(25) Crescenzi, V.; Manzini, G.; Calzolari, G.; Borri, C. *Eur. Polym. J.* **1972**, *8*, 449.
(26) Chatani, Y.; Okita, Y.; Tadokoro, H.; Yamashita, Y. *Polym. J.* **1970**, *1*, 555.
(27) Ueki, T.; Hiragi, Y.; Kataoka, M.; Inoko, Y.; Amemiya, Y.; Izumi, Y.; Tagawa, H.; Muroga, Y. *Biophys. Chem.* **1985**, *23*, 115.
(28) Nojima, S.; Hashizume, K.; Rohadi, A.; Sasaki, S. *Polymer* **1997**, *38*, 2711.
(29) Ruland, W. *J. Appl. Crystallogr.* **1971**, *4*, 70.
(30) Feigin, L. A.; Svergun, D. I. *Structure Analysis by Small-Angle X-ray and Neutron Scattering*; Plenum Press: New York, 1987.
(31) deGennes, P. G. *Scaling Concepts in Polymer Physics*; Cornell University Press: Ithaca, NY, 1979.
(32) Vavasour, J. D.; Whitmore, M. D. *Macromolecules* **1992**, *25*, 5477.
(33) Wunderlich, B. *Macromolecular Physics;* Vols 1−3; Academic Press: London, 1973−1980.
(34) Phillips, P. J.; Rensch, G. J.; Taylor K. D. J. Polym. Sci. **1987**, *B25*, 1725.
(35) Ito, K.; Yamashita, Y. *Macromolecules* **1978**, *11*, 68.

MA981708P